

New Benchmark for Water Photooxidation by Nanostructured  $\alpha$ -Fe<sub>2</sub>O<sub>3</sub> Films

Andreas Kay, Ilkay Cesar, and Michael Grätzel\*

*Contribution from the Institut des sciences et ingénierie chimiques, Ecole Polytechnique Fédérale de Lausanne, CH-1015 Lausanne, Switzerland*

Received June 21, 2006; E-mail: michael.graetzel@epfl.ch

**Abstract:** Thin films of silicon-doped Fe<sub>2</sub>O<sub>3</sub> were deposited by APCVD (atmospheric pressure chemical vapor deposition) from Fe(CO)<sub>5</sub> and TEOS (tetraethoxysilane) on SnO<sub>2</sub>-coated glass at 415 °C. HRSEM reveals a highly developed dendritic nanostructure of 500 nm thickness having a feature size of only 10–20 nm at the surface. Real surface area determination by dye adsorption yields a roughness factor of 21. XRD shows the films to be pure hematite with strong preferential orientation of the [110] axis vertical to the substrate, induced by silicon doping. Under illumination in 1 M NaOH, water is oxidized at the Fe<sub>2</sub>O<sub>3</sub> electrode with higher efficiency (IPCE = 42% at 370 nm and 2.2 mA/cm<sup>2</sup> in AM 1.5 G sunlight of 1000 W/m<sup>2</sup> at 1.23 V<sub>RHE</sub>) than at the best reported single crystalline Fe<sub>2</sub>O<sub>3</sub> electrodes. This unprecedented efficiency is in part attributed to the dendritic nanostructure which minimizes the distance photogenerated holes have to diffuse to reach the Fe<sub>2</sub>O<sub>3</sub>/electrolyte interface while still allowing efficient light absorption. Part of the gain in efficiency is obtained by depositing a thin insulating SiO<sub>2</sub> interfacial layer between the SnO<sub>2</sub> substrate and the Fe<sub>2</sub>O<sub>3</sub> film and a catalytic cobalt monolayer on the Fe<sub>2</sub>O<sub>3</sub> surface. A mechanistic model for water photooxidation is presented, involving stepwise accumulation of four holes by two vicinal iron or cobalt surface sites.

## Introduction

Nature found a way to split water into hydrogen and oxygen by sunlight some 3 billion years ago when cyanobacteria evolved.<sup>1</sup> Photosynthesis based on two photosystems connected in series thus became the primary source of energy for nearly all forms of life on earth. Even fossil fuels owe their existence to the utilization of solar energy by plants hundreds of million years ago. Mankind has been trying to imitate natural photosynthesis, hoping to find an alternative for nonrenewable and polluting fossil fuels. Sunlight can be transformed into electrical energy by photovoltaic cells and then stored as chemical energy in a battery or in the form of hydrogen by electrolysis of water. The direct photoelectrolysis of water by light was first achieved with a TiO<sub>2</sub> photoelectrode for oxygen evolution connected to a platinum counter electrode for hydrogen evolution.<sup>2</sup> However, this single photon system requires a light energy of at least 3.0 eV, the band gap of TiO<sub>2</sub> (rutile), so that only a small fraction of the solar spectrum (light below 420 nm) can be utilized. Although the standard free enthalpy for water splitting is just 1.23 eV per electron, at least twice the photon energy is needed for a single photon system, since two electrons have to be transferred per water molecule.<sup>3</sup> Harvesting the visible part of the solar spectrum is only possible with a two (or more) photon system, as in natural photosynthesis.<sup>4</sup> This can be achieved for example in a tandem configuration by connecting a larger band

gap semiconductor photoanode for oxygen evolution (such as WO<sub>3</sub> with  $E_g = 2.5$  eV or Fe<sub>2</sub>O<sub>3</sub> with  $E_g = 2.1$  eV) in series with two dye-sensitized solar cells and a hydrogen-evolving cathode.<sup>5</sup> Red and green light transmitted by the photoanode are absorbed by the dye, so that a large part of the solar spectrum can be utilized.

Iron oxide ( $\alpha$ -Fe<sub>2</sub>O<sub>3</sub>, or hematite) is especially attractive as a photoanode due to its abundance, stability, and environmental compatibility, as well as suitable band gap and valence band edge position. Unfortunately, the reported efficiencies of water oxidation at illuminated hematite electrodes are notoriously low. White light photocurrents given in the literature are difficult to compare, because they are very sensitive to the spectral distribution of the illumination source.<sup>6</sup> We shall therefore compare the published monochromatic incident photon to current efficiencies (IPCEs) at an electrode potential given relative to the reversible hydrogen electrode (RHE) at the pH of the employed electrolyte (in most cases 0.1 or 1 M NaOH). The reversible oxygen electrode has a potential of 1.23 V<sub>RHE</sub>, and any additional voltage applied to the Fe<sub>2</sub>O<sub>3</sub> electrode corresponds to an overvoltage for oxygen evolution.

So far the highest IPCE was probably obtained with 1.5% niobium-doped  $\alpha$ -Fe<sub>2</sub>O<sub>3</sub> single crystals (IPCE = 37% at 370 nm and 1.23 V<sub>RHE</sub>).<sup>7,8</sup> Sintered polycrystalline electrodes are

- (1) Des Marais, D. J. *Science* **2000**, 289, 1703–1705.
- (2) Fujishima, A.; Honda, K. *Nature* **1972**, 238, 37.
- (3) Bolton, J. R.; Strickler, S. J.; Connolly, J. S. *Nature* **1985**, 316, 495–500.
- (4) Nozik, A. J. *Appl. Phys. Lett.* **1977**, 30, 567–569.

- (5) Duret, A.; Grätzel, M. *J. Phys. Chem. B* **2005**, 109, 17184–17191.
- (6) Murphy, A. B.; Barnes, P. R. F.; Randeniya, L. K.; Plumb, I. C.; Grey, I. E.; Horne, M. D.; Glasscock, J. A. *Int. J. Hydrogen Energy* **2006**, 31, 1999–2017.
- (7) Sanchez, C.; Hendewerk, M.; Sieber, K. D.; Somorjai, G. A. *J. Solid State Chem.* **1986**, 61, 47–55.

less efficient,<sup>9–11</sup> with the exception of 2% silicon-doped hematite (IPCE = 34% at 400 nm and 1.23 V<sub>RHE</sub>),<sup>12</sup> although much lower values had been reported for the same electrodes in a previous paper (IPCE = 5% at 400 nm and 1.49 V<sub>RHE</sub>).<sup>13</sup> Thin film electrodes of  $\alpha$ -Fe<sub>2</sub>O<sub>3</sub> were prepared by chemical vapor deposition (CVD),<sup>14,15</sup> by reactive sputtering<sup>16,17</sup> (IPCE = 21% at 400 nm and 1.46 V<sub>RHE</sub>),<sup>16</sup> and more often by spray coating on SnO<sub>2</sub>-glass,<sup>18–23</sup> giving quantum efficiencies up to IPCE = 25% at 400 nm and 1.42 V<sub>RHE</sub>.<sup>23</sup>

The poor efficiency of  $\alpha$ -Fe<sub>2</sub>O<sub>3</sub> photoanodes has been attributed to a low rate constant of water oxidation by surface trapped holes<sup>24</sup> and a short hole diffusion length in hematite (20 nm,<sup>24</sup> 2–4 nm<sup>25</sup>) which allows only holes created close to the electrolyte interface to oxidize water. Since the light penetration length in  $\alpha$ -Fe<sub>2</sub>O<sub>3</sub> is of the order of 100 nm ( $\alpha$  =  $1.6 \times 10^7 \text{ m}^{-1}$  at 500 nm),<sup>26</sup> most holes are created in the bulk and will recombine with electrons before having reached the surface. It has been proposed to stack several very thin films of  $\alpha$ -Fe<sub>2</sub>O<sub>3</sub> in order to minimize hole transfer distances while still absorbing most of the incident light.<sup>18,19,22</sup> This approach is reminiscent of the stacking of chlorophyll-containing thylakoid membranes in the grana of plant chloroplasts.<sup>27</sup> Similar effects can be achieved with a nanostructured electrode using a porous film of interconnected nanocrystalline hematite particles.<sup>28,29</sup> While sintered thin films of undoped colloidal hematite on conducting SnO<sub>2</sub> glass produced IPCEs below 1%,<sup>30</sup> sol–gel films of Fe<sub>2</sub>O<sub>3</sub> containing 25% niobium gave up to 8% IPCE at 380 nm and 1.17 V<sub>RHE</sub>.<sup>31</sup> Undoped arrays of vertically aligned  $\alpha$ -Fe<sub>2</sub>O<sub>3</sub> nanorods grown from aqueous solution on SnO<sub>2</sub> glass again showed low photocurrents.<sup>32</sup> Similar arrays of vertically aligned hematite nanowires can also be obtained by thermal oxidation of iron.<sup>33–39</sup> These nanostructures, if doped,<sup>39</sup> might prove very interesting as water splitting photoanodes.

Ultrasonic spray coating of  $\alpha$ -Fe<sub>2</sub>O<sub>3</sub> on SnO<sub>2</sub> glass also produces nanostructured layers, and results in higher water splitting efficiencies (IPCE = 16% at 370 nm and 1.2 V<sub>RHE</sub>).<sup>5</sup> In a recent communication we reported that silicon doping of hematite is essential not only for electrical conductivity but also for the highly developed nanostructure of the film.<sup>40</sup> Further, we presented a new technique for film preparation by atmospheric pressure chemical vapor deposition (APCVD) with iron pentacarbonyl Fe(CO)<sub>5</sub> as precursor. Here we present a detailed account on further remarkable progress with silicon-doped hematite films obtained by APCVD, now reaching photoconversion efficiencies even higher than those of single crystals.

## Experimental Section

**Film Preparation by APCVD.** Glass coated with fluorine-doped SnO<sub>2</sub> (TEC 15, Hartford Glass Co., 15  $\Omega$ /square, 50  $\times$  13  $\times$  2.3 mm<sup>3</sup>) cleaned with acetone and Milli-Q water was used as substrate. An aluminum block (50  $\times$  25  $\times$  12 mm<sup>3</sup>) with an incorporated 125 W heating element served as a substrate heater. Its temperature was measured by an inserted thermocouple and regulated to 450 °C (lower temperatures gave less efficient photoelectrodes; above 470 °C the deposition efficiency decreased rapidly). The temperature measured on the SnO<sub>2</sub> glass surface with a thin thermocouple (type K, wire  $\varnothing$  = 0.13 mm, attached with solder glass Schott G 017–340) was about 420 °C in still air and 415 °C during APCVD. The precursors Fe(CO)<sub>5</sub> (Aldrich 99.999%, vapor pressure  $P(25^\circ\text{C})$  = 29 Torr)<sup>41</sup> and tetraethoxysilane (TEOS, Aldrich 99.999%,  $P(25^\circ\text{C})$  = 1.5 Torr)<sup>42</sup> were supplied by bubbling argon gas (99.9999%, 11.3 mL/min for Fe(CO)<sub>5</sub> and 19.4 mL/min for TEOS at 25 °C, metered by thermal mass flow controllers) through 0.5 mL of each liquid. The precursor flow rate determined from the weight loss of the bubblers agrees with that calculated from the vapor pressures and argon flow rates (Fe(CO)<sub>5</sub>: 3.5 mg/min and TEOS: 0.32 mg/min, corresponding to 8 mol % of Si). Lower TEOS concentrations yielded less efficient photoelectrodes, while higher ones gave inactive brown instead of red brown films. These two vapor streams were mixed with air (2 L/min, purified over molecular sieve 5A and a 0.22  $\mu\text{m}$  Millipore filter) and directed vertically onto the substrate through a glass tube of 13 mm inner diameter from a distance of 20 mm. Within 5 min a circular spot of Fe<sub>2</sub>O<sub>3</sub> was deposited on the SnO<sub>2</sub> substrate showing concentric interference fringes in reflected light indicating a radial thickness profile. The preparation of homogeneous films on large substrates would require long slit nozzles and a continuously moving substrate, as in the industrial deposition of the SnO<sub>2</sub> coating on the glass substrate in a moving belt APCVD reactor.<sup>43</sup> Deposition of Fe<sub>2</sub>O<sub>3</sub> could easily be implemented as a second step in the same continuous coating process.

Improved electrode performance was achieved when an interfacial layer of SiO<sub>2</sub> was first deposited for 5 min on SnO<sub>2</sub> under the same conditions but with TEOS only, followed by Fe<sub>2</sub>O<sub>3</sub> deposition. All experiments involving Fe(CO)<sub>5</sub> were done under a fume hood due to its toxicity.

- (8) Sanchez, C.; Sieber, K. D.; Somorjai, G. A. *J. Electroanal. Chem.* **1988**, 252, 269–290.
- (9) Sanchez, H. L.; Steinfink, H.; White, H. S. *J. Solid State Chem.* **1982**, 41, 90–96.
- (10) Turner, J. E.; Hendewerk, M.; Parmeter, J.; Neiman, D.; Somorjai, G. A. *J. Electrochem. Soc.* **1984**, 131, 1777–1783.
- (11) Shakhnazaryan, G. E.; Sarkisyan, A. G.; Arutyunyan, V. M.; Arakelyan, V. M.; Turner, J. A.; Vartanyan, R. S. *Russ. J. Electrochem.* **1994**, 30, 610–614.
- (12) Shinar, R.; Kennedy, J. H. *Sol. Energy Mater.* **1982**, 6, 323–335.
- (13) Kennedy, J. H.; Anderman, M.; Shinar, R. *J. Electrochem. Soc.* **1981**, 128, 2371–2373.
- (14) Hardee, K. L.; Bard, A. J. *J. Electrochem. Soc.* **1976**, 123, 1024–1026.
- (15) Hardee, K. L.; Bard, A. J. *J. Electrochem. Soc.* **1977**, 124, 215–224.
- (16) Schumacher, L. C.; McIntyre, N. S.; Mamicheafara, S.; Dignam, M. J. *J. Electroanal. Chem.* **1990**, 277, 121–138.
- (17) Miller, E. L.; Paluselli, D.; Marsen, B.; Rocheleau, R. E. *Sol. Energy Mater. Sol. Cells* **2005**, 88, 131–144.
- (18) Itoh, K.; Bockris, J. O. *J. Appl. Phys.* **1984**, 56, 874–876.
- (19) Itoh, K.; Bockris, J. O. *J. Electrochem. Soc.* **1984**, 131, 1266–1271.
- (20) Majumder, S. A.; Khan, S. U. M. *Int. J. Hydrogen Energy* **1994**, 19, 881–887.
- (21) Khan, S. U. M.; Akikusa, J. *J. Phys. Chem. B* **1999**, 103, 7184–7189.
- (22) Jorand Sartoret, C.; Ulmann, M.; Alexander, B. D.; Augustynski, J.; Weidenkaff, A. *Chem. Phys. Lett.* **2003**, 376, 194–200.
- (23) Jorand Sartoret, C.; Alexander, B. D.; Solarska, R.; Rutkowska, I. A.; Augustynski, J.; Cerny, R. *J. Phys. Chem. B* **2005**, 109, 13685–13692.
- (24) Dare-Edwards, M. P.; Goodenough, J. B.; Hammett, A.; Trevellick, P. R. *J. Chem. Soc., Faraday Trans. I* **1983**, 79, 2027–2041.
- (25) Kennedy, J. H.; Frese, K. W. *J. Electrochem. Soc.* **1978**, 125, 709–714.
- (26) Gardner, R. F. G.; Sweett, F.; Tanner, D. W. *J. Phys. Chem. Solids* **1963**, 24, 1183–1186.
- (27) Kay, A.; Grätzel, M. *J. Phys. Chem.* **1993**, 97, 6272–6277.
- (28) Hodes, G.; Howell, I. D. J.; Peter, L. M. *J. Electrochem. Soc.* **1992**, 139, 3136–3140.
- (29) Hagfeldt, A.; Grätzel, M. *Chem. Rev.* **1995**, 95, 49–68.
- (30) Björkstén, U.; Moser, J.; Grätzel, M. *Chem. Mater.* **1994**, 6, 858–863.
- (31) Miyake, H.; Kozuka, H. *J. Phys. Chem. B* **2005**, 109, 17951–17956.
- (32) Lindgren, T.; Wang, H. L.; Beermann, N.; Vayssieres, L.; Hagfeldt, A.; Lindquist, S. E. *Sol. Energy Mater. Sol. Cells* **2002**, 71, 231–243.
- (33) Takagi, R. *J. Phys. Soc. Jpn.* **1957**, 12, 1212–18.

- (34) Fu, Y. Y.; Chen, J.; Zhang, H. *Chem. Phys. Lett.* **2001**, 350, 491–494.
- (35) Fu, Y. Y.; Wang, R. M.; Xu, J.; Chen, J.; Yan, Y.; Narlikar, A. V.; Zhang, H. *Chem. Phys. Lett.* **2003**, 379, 373–379.
- (36) Wen, X. G.; Wang, S. H.; Ding, Y.; Wang, Z. L.; Yang, S. H. *J. Phys. Chem. B* **2005**, 109, 215–220.
- (37) Wang, R. M.; Chen, Y. F.; Fu, Y. Y.; Zhang, H.; Kisielowski, C. *J. Phys. Chem. B* **2005**, 109, 12245–12249.
- (38) Xu, Y. Y.; Rui, X. F.; Fu, Y. Y.; Zhang, H. *Chem. Phys. Lett.* **2005**, 410, 36–38.
- (39) Fan, Z. Y.; Wen, X. G.; Yang, S. H.; Lu, J. G. *Appl. Phys. Lett.* **2005**, 87, Art. No. 013113.
- (40) Cesar, I.; Kay, A.; Gonzalez Martinez, J. A.; Grätzel, M. *J. Am. Chem. Soc.* **2006**, 128, 4582–4583.
- (41) Gilbert, A. G.; Sulzmann, K. G. *J. Electrochem. Soc.* **1974**, 121, 832–834.
- (42) Alcott, G. R.; van de Sanden, R. M. C. M.; Kondic, S.; Linden, J. L. *Chem. Vap. Deposition* **2004**, 10, 20–22.
- (43) Grelenski, N. M. In *Lawrence Berkeley Lab.: Transparent Heat-Mirror Mater. and Deposition Technol.* **1982**, 79–98.

**SEM.** The morphology of Si-doped and undoped hematite films was characterized using a high-resolution scanning electron microscope equipped with a field emission gun (Philips XL-SFEG). The acceleration voltage was 5 keV while an in-lens detector was employed with a working distance of 5 mm. Film cross-section images were obtained from cleaved samples. The samples were investigated after the photoelectrochemical measurements and sample positions coincide with the illuminated area.

**XRD.** X-ray diffraction patterns of  $\text{Fe}_2\text{O}_3$  films with a  $\text{SiO}_2$  interfacial layer on  $\text{SnO}_2$  glass substrate were measured with a PANalytical X'Pert Pro using  $\text{Cu K}\alpha_1$  radiation (0.1540 nm) at an incident angle of  $1/4^\circ$ , scanning detector with  $2.12^\circ$  collecting length, step size  $0.008^\circ$ , 250 s per step.<sup>44</sup>

**XEDS/TEM.** X-ray energy dispersive spectroscopy for elemental analysis was performed using a Hitachi HF-2000 TEM equipped with a XEDS spectrometer (Voyager-Tracor-Northern/Noran) and a high purity germanium X-ray detector (HPGe) with a take off angle of  $49.51^\circ$ , operated at 200 keV in dark field scanning transmission electron microscopy mode. Material of undoped and silicon-doped samples were scratched off the surface with a razor blade and transferred onto a holey carbon thin film supported by a copper grid. Per sample several areas of  $150 \text{ nm}^2$  were scanned with a lifetime of 130 s. To exclude artifacts from the support, a background signal was obtained probed next to the sample material. The background signal contained only carbon and copper.

**Roughness Factor.** The real surface area of the  $\text{Fe}_2\text{O}_3$  films as compared to their macroscopic surface was determined by adsorption of the azo-dye Orange II, which has been shown to form a monolayer on nanocrystalline  $\alpha\text{-Fe}_2\text{O}_3$  at a concentration of 1.5 mM in water of pH 3.5, occupying an area of  $0.40 \text{ nm}^2$  per dye molecule.<sup>45</sup>  $\text{Fe}_2\text{O}_3$  electrodes of  $0.5 \text{ cm}^2$  macroscopic surface area were exposed for 15 min to the dye solution, the adsorbed dye desorbed with 0.5 mL of 1 M NaOH, and its concentration was determined from the optical density at 450 nm.

**UV-vis spectra** of the  $\text{Fe}_2\text{O}_3$  films were taken with a Hewlett-Packard 8452A diode array spectrophotometer. To reduce light reflection at the  $\text{Fe}_2\text{O}_3$  surface, and to approach the conditions in the photoelectrochemical cell, the films were wetted with water and covered with a microscopy cover glass. The  $\text{SnO}_2$  substrate without the  $\text{Fe}_2\text{O}_3$  coating served as a blank.

**Photoelectrochemical Characterization.** Photocurrents were measured in a three-electrode configuration with 1 M NaOH (Fluka, pro analysi in Milli-Q water,  $25^\circ\text{C}$ , pH = 13.6)<sup>46</sup> as electrolyte,  $\text{Ag}/\text{AgCl}/\text{sat. KCl}$  as reference, and a platinum wire as counter electrode, separated by glass frits. Contact to the  $\text{SnO}_2$  substrate of the  $\text{Fe}_2\text{O}_3$  film was made with a titanium clip above the electrolyte. The potential of the photoelectrode was controlled by a potentiostat (PAR 273A) and is reported against the reversible hydrogen electrode (RHE):

$$E_{\text{RHE}} = E_{\text{AgCl}} + 0.059 \text{ pH} + E_{\text{AgCl}}^\circ \quad \text{with } E_{\text{AgCl}}^\circ = 0.1976 \text{ V at } 25^\circ\text{C}$$

The  $\text{Fe}_2\text{O}_3$  film was illuminated through 6 mm of electrolyte and a fused silica window with a  $0.5 \text{ cm}^2$  circular mask, the total surface immersed into the electrolyte being about  $2.5 \text{ cm}^2$ . Sunlight was simulated with a 450 W xenon lamp (Osram, ozone free) by removing infrared ( $>720 \text{ nm}$ ) and short UV light ( $<320 \text{ nm}$ ) with a KG3 filter (3 mm, Schott) and adjusting the light intensity so that a Si photodiode covered with another KG3 filter gave the same photocurrent as that in global AM 1.5<sup>47</sup> sunlight of  $1000 \text{ W/m}^2$ . Photocurrent action spectra were obtained under light from a 300 W Xe lamp with an integrated parabolic reflector (Cermox PE 300 BUV) passing through a mono-

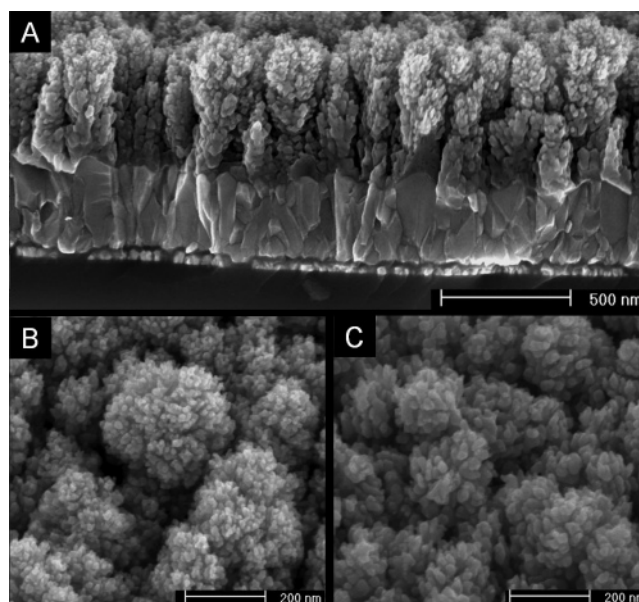


**Figure 1.** HR-SEM images of  $\text{Fe}_2\text{O}_3$  films grown by APCVD on  $\text{SnO}_2$ :F-coated conducting glass. (A) Cross-section of 500 nm thick mesoporous Si-doped  $\text{Fe}_2\text{O}_3$  on 400 nm thick compact  $\text{SnO}_2$ :F. (B) Top view ( $45^\circ$  tilted) of the Si-doped  $\text{Fe}_2\text{O}_3$  film. (C) Top view ( $45^\circ$  tilted) of an undoped  $\text{Fe}_2\text{O}_3$  film.

chromator (Bausch & Lomb, bandwidth 10 nm fwhm). The wavelength was scanned at 1 nm/s, and the monochromatic photocurrent of the  $\text{Fe}_2\text{O}_3$  electrode compared with that of a UV enhanced Si-photodiode (Oriol 71883) of known IPCE spectrum. The monochromatic light intensity was high enough (e.g.,  $59 \text{ W/m}^2$  at 400 nm) to yield a photocurrent of 100 to  $700 \mu\text{A/cm}^2$  between 310 and 570 nm. In this range the photocurrent of the  $\text{Fe}_2\text{O}_3$  electrode is proportional to light intensity and its dark current ( $1 \mu\text{A/cm}^2$ ) is negligible compared to the photocurrent.

**XPS.** X-ray photoelectron spectroscopy was performed on a Kratos Axis Ultra spectrometer with an Al anode (Al  $\text{K}\alpha$ : 1486.6 eV). A surface area of  $700 \times 350 \mu\text{m}^2$  was analyzed at a takeoff angle of  $90^\circ$ . The C 1s contamination peak was used as reference and adjusted to 285 eV.<sup>48</sup>

## Results and Discussion

**Film Morphology.** Figure 1 compares the morphology of silicon-doped (Figure 1A and B) and undoped (Figure 1C) hematite films. The cross-section of the silicon-doped film (Figure 1A) shows the 400 nm thick substrate layer of  $\text{SnO}_2$ :F on which a 500 nm thick mesoporous  $\text{Fe}_2\text{O}_3$  film is grown. With a deposition time of 5 min this corresponds to an APCVD growth rate of 100 nm/min. The film consists of perpendicularly oriented dendritic structures with more finely divided branches toward the surface of the film. The topmost nanocrystals have a diameter between 10 and 20 nm for the Si-doped sample. In the undoped sample the particle size is considerably larger with 20 to 40 nm. The width of the more compact stems of the dendrites varies between 75 and 250 nm. From the cross-sectional view it becomes apparent that the gaps between the dendrites reach deep into the film, exposing also the internal surface of the  $\text{Fe}_2\text{O}_3$  film to the electrolyte.

**XRD Spectroscopy.** The X-ray diffraction pattern of the Si-doped  $\text{Fe}_2\text{O}_3$  film (with  $\text{SiO}_2$  interfacial layer) in Figure 2a

(44) XRD patterns were kindly provided by Dr. V. Shklover, Laboratory of Crystallography, ETHZ, Zürich, Switzerland.

(45) Bandara, J.; Mielczarski, J. A.; Kiwi, J. *Langmuir* **1999**, *15*, 7670–7679.

(46) Kennedy, J. H.; Frese, K. W. *J. Electrochem. Soc.* **1978**, *125*, 723–726.

(47) <http://redc.nrel.gov/solar/spectra/am1.5/>.

(48) XPS data were kindly provided by N. Xanthopoulos, Laboratory of Metallurgical Chemistry, EPFL, Lausanne, Switzerland.



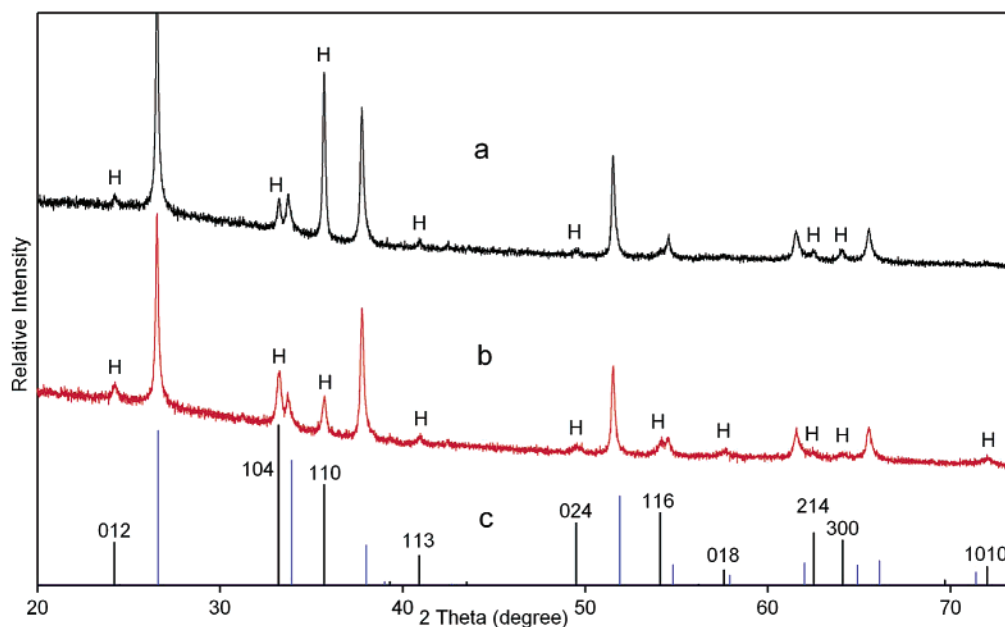


**Figure 2.** X-ray diffraction pattern of (a) Si-doped Fe<sub>2</sub>O<sub>3</sub> film on SnO<sub>2</sub> (hematite peaks marked with H), (b) undoped Fe<sub>2</sub>O<sub>3</sub> film on SnO<sub>2</sub>, (c) standard powder pattern of  $\alpha$ -Fe<sub>2</sub>O<sub>3</sub> (hematite, black lines with plane indices in hexagonal coordinates) and SnO<sub>2</sub> (cassiterite, blue lines).

shows mainly diffraction peaks from the dense SnO<sub>2</sub> coating of the glass substrate (0.4  $\mu$ m cassiterite, Figure 2c). There is only one strong peak due to  $\alpha$ -Fe<sub>2</sub>O<sub>3</sub> (hematite), namely the (110) reflection (in hexagonal coordinates), besides much weaker peaks corresponding to the (012), (104), (113), (024), (214), and (300) planes. Other phases of iron oxide are not apparent. A similar prevalence of the (110) reflection has also been observed for  $\alpha$ -Fe<sub>2</sub>O<sub>3</sub> nanowires and nanobelts grown by thermal oxidation of iron<sup>33–37</sup> and indicates a strong preferential orientation of the [110] axis vertical to the substrate.

The crystallite size estimated from the broadening of the (110) peak by the Scherrer equation is 15.5 nm, in accordance with the average grain size in SEM and TEM.

The intensity distribution in the XRD pattern of the undoped Fe<sub>2</sub>O<sub>3</sub> film (Figure 2b) corresponds to the standard powder pattern of hematite (Figure 2c), with the stronger (104) reflection and smaller (110) and (116) peaks. Hence the preferential orientation of the Si-doped Fe<sub>2</sub>O<sub>3</sub> film is induced by the presence of TEOS during APCVD.<sup>49</sup>

The hematite lattice can be represented as an alternation of iron bilayers and oxygen layers parallel to the (001) basal plane as illustrated in Figure 3. Fe<sup>III</sup> atoms within each bilayer have parallel spins, while adjacent bilayers have opposite spins. Electrons can move by hopping through Fe<sup>II</sup>/Fe<sup>III</sup> valence change within the iron bilayers, while electron exchange between neighboring bilayers is spin forbidden (Hund's rule).<sup>50</sup> This is the classical explanation for the strongly anisotropic conductivity of hematite, which is up to 4 orders of magnitude higher within the (001) basal plane (e.g., in [110] direction) than orthogonal to them. A more thorough quantum mechanical interpretation of the conductivity anisotropy of hematite has been given recently.<sup>50</sup> By contrast valence band hole transfer between adjacent iron double layers is spin-allowed through Fe<sup>III/IV</sup>

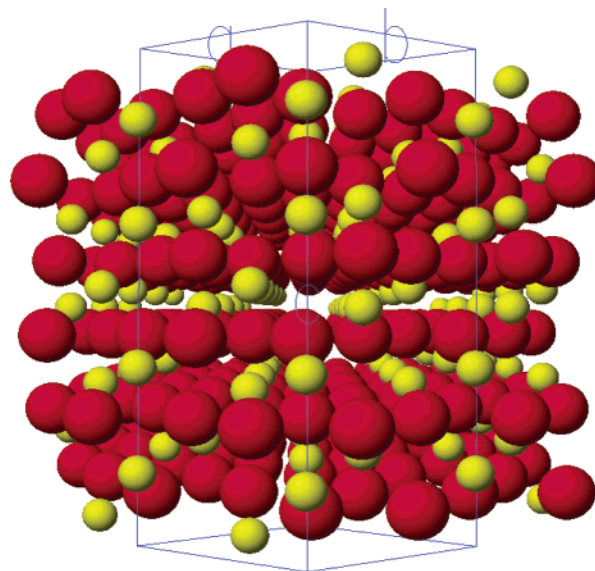


**Figure 3.** Model of the hematite crystal lattice viewed in [110] direction, which is preferentially oriented vertically on the SnO<sub>2</sub> substrate, illustrating alternating iron bilayers and oxygen layers parallel to the (001) basal plane (oxygen, red; iron, yellow; hexagonal unit cell, blue).

valence change and, hence, can proceed albeit with a higher activation barrier than that within the iron planes.<sup>50</sup>

Preferential orientation of the well conducting (001) plane vertically to the substrate should facilitate collection of photo-generated electrons. At the same time photogenerated holes can still hop laterally between (001) planes to reach the electrolyte interface. On the other hand, niobium-doped single crystals platelets of  $\alpha$ -Fe<sub>2</sub>O<sub>3</sub> show good efficiency for water oxidation with only the (001) basal plane exposed to the electrolyte,<sup>8</sup> which implies electron transport vertically to (001). Apparently in this case the conductivity of niobium-doped  $\alpha$ -Fe<sub>2</sub>O<sub>3</sub> was sufficient even in the [001] direction to allow collection of photogenerated electrons.

**Si-Doping Level.** The silicon content in the hematite film was below the detection limit of XEDS/SEM at an acceleration

(49) Campbell, A. S.; Schwertmann, U.; Stanjek, H.; Friedl, J.; Kyek, A.; Campbell, P. A. *Langmuir* **2002**, *18*, 7804–7809.

(50) Jordanova, N.; Dupuis, M.; Rosso, K. M. *J. Chem. Phys.* **2005**, *122*, Art. No. 144305.

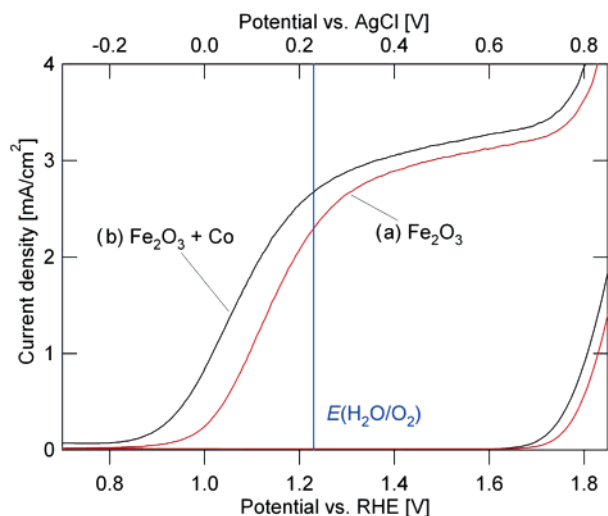


**Figure 4.** Current–voltage characteristics in darkness and under simulated sunlight at a scan rate of 50 mV/s. (a) Unmodified  $\text{Fe}_2\text{O}_3$ ; (b) the same electrode after cobalt treatment.

voltage of 5 keV, which is the upper limit to prevent interference from the glass substrate. However, silicon was clearly detected by XEDS/TEM at 200 keV in hematite particles scratched off the substrate at a level of 1.5 at. % Si, as compared to <0.1 at. % Si for the undoped film. The doping level is much lower than the TEOS concentration during APCVD (8 mol %), due to the very low reactivity of TEOS compared to  $\text{Fe}(\text{CO})_5$  at 415 °C.<sup>51,52</sup>

**Roughness Factor.** The real surface area of the hematite films as compared to the macroscopic surface area determined by dye adsorption (Orange II) on five samples is  $\text{RF} = 21 \pm 2$ .

**Photocurrent–Voltage Characteristics.** Figure 4a shows the current–voltage ( $I$ – $V$ ) curve of a silicon-doped hematite electrode with a  $\text{SiO}_2$  interfacial layer in darkness and in simulated sunlight. The dark current is negligible up to about 1.6  $V_{\text{RHE}}$ , where electrocatalytic oxygen evolution starts (the dark current of the  $\text{SnO}_2$  substrate is negligible up to 1.8  $V_{\text{RHE}}$  and unaffected by the  $\text{SiO}_2$  coating). The photocurrent rises steeply between 1.0 and 1.2  $V_{\text{RHE}}$  leveling off before the dark current sets in. At 1.23  $V_{\text{RHE}}$  (corresponding to the potential of the reversible oxygen electrode) the photocurrent density is 2.3  $\text{mA}/\text{cm}^2$ , 65% higher than in our previous report.<sup>40</sup>

Without silicon doping the photocurrent is in the order of 10  $\mu\text{A}/\text{cm}^2$  at 1.23  $V_{\text{RHE}}$  (undoped  $\alpha\text{-Fe}_2\text{O}_3$  is an insulator).<sup>53</sup> Thermal oxidation of  $\text{Fe}(\text{CO})_5$  yields  $\text{Fe}_2\text{O}_3$  of high purity, since iron pentacarbonyl decomposes easily to atomic iron and carbon monoxide, which is not expected to be incorporated into the hematite lattice.<sup>54,55</sup> By contrast, other precursors commonly employed in deposition of  $\text{Fe}_2\text{O}_3$  films, such as  $\text{Fe}(\text{acac})_3$ <sup>5,40</sup> and  $\text{FeCl}_3$ ,<sup>18–23</sup> may leave carbon or chlorine residues in the film that can act as electron donors. This would explain why such films give appreciable photocurrents even when no dopant was added intentionally.

**$\text{SiO}_2$  Interfacial Layer.**  $\text{Fe}_2\text{O}_3$  films directly deposited on the  $\text{SnO}_2$  substrate without a  $\text{SiO}_2$  interfacial layer give lower and poorly reproducible photocurrents. Thin insulating layers of  $\text{SiO}_2$  are widely used in metal–insulator–semiconductor (MIS) devices, such as MIS solar cells,<sup>56,57</sup> as well as electroluminescent devices, such as OLEDs.<sup>58</sup> Deposition with TEOS as precursor is usually done at low pressure (LPCVD) and temperatures exceeding 600 °C or with plasma enhancement or ozone. Under our experimental conditions (APCVD at 415 °C) deposition is very slow.<sup>51,52</sup> However, formation of the first monolayer should be rapid, due to reaction of the ethoxyl groups of TEOS with surface hydroxyl groups on  $\text{SnO}_2$ .<sup>59</sup>

We confirmed deposition of an ultrathin layer of  $\text{SiO}_2$  on  $\text{SnO}_2$  by XPS (Si 2p peak at 102.5 eV binding energy and two distinct O 1s peaks at 531 and 533 eV, attributable to  $\text{SnO}_2$  and  $\text{SiO}_2$ ).<sup>60</sup> The substrate Sn 3d<sub>5/2</sub> peak (binding energy 487 eV, kinetic energy 1000 eV) was attenuated by a factor of 0.6 after  $\text{SiO}_2$  deposition, indicating a layer thickness on the order of 1 nm, the exact value depending on the escape depth taken for 1 keV photoelectrons in  $\text{SiO}_2$ .<sup>59,61</sup>

Electrons from the hematite film can tunnel through such a thin layer of  $\text{SiO}_2$ , as in the case of MIS junctions. Ideally the contact between  $\text{SnO}_2$  substrate and  $\alpha\text{-Fe}_2\text{O}_3$  should be ohmic, which is expected to be the case, since the work function of  $\text{SnO}_2\text{:F}$  ( $\Phi \approx 4.8$  eV)<sup>62</sup> is lower than that estimated for hematite ( $\Phi \approx 5.6$  eV).<sup>63</sup> However, the electronic structure of the  $\text{SnO}_2/\text{Fe}_2\text{O}_3$  contact may be influenced by fixed charges in interface states.<sup>56,58</sup> As in MIS and electroluminescent devices the beneficial effect of a thin insulating layer could be due to an improved energy level alignment at the interface. The  $\text{SiO}_2$  layer may also affect the nucleation of hematite on the substrate. Further investigations are required to optimize and rationalize the interfacial layer effect.

**Water Oxidation Catalysis by Cobalt.** Following photoelectrochemical characterization the electrode of Figure 4a was rinsed with Milli-Q water, dried in a stream of air, treated with 10  $\mu\text{L}/\text{cm}^2$  of 10 mM  $\text{Co}(\text{NO}_3)_2$ , rinsed with water after a few seconds, and measured again (Figure 4b). The cobalt treatment results in an 80 mV cathodic shift, and the photocurrent at 1.23  $V_{\text{RHE}}$  increases to 2.7  $\text{mA}/\text{cm}^2$ . A slightly smaller gain is seen after a single treatment with 10  $\mu\text{L}/\text{cm}^2$  of 1 mM  $\text{Co}(\text{NO}_3)_2$ , but a second application gives the full improvement. Further treatments or higher concentrations yield no additional enhancement. Neutralization of adsorbed NaOH residues left from the first measurement on the  $\alpha\text{-Fe}_2\text{O}_3$  film with 1 M  $\text{HNO}_3$  before cobalt treatment gives the same result, indicating that  $\text{Co}(\text{OH})_2$  precipitation due to a basic hematite surface is not required.  $\text{Co}^{\text{II}}$  adsorption on hematite has indeed been found to start around neutral pH, below the point of zero charge ( $\text{pH}_{\text{pzc}} = 8.5$ ).<sup>64</sup> In the case of a single treatment with 10  $\mu\text{L}/\text{cm}^2$  of 1

- (51) Adachi, M.; Okuyama, K.; Tohge, N.; Shimada, M.; Sato, J.; Muroyama, M. *Jpn. J. Appl. Phys.* **1993**, *32*, L748–L751.  
 (52) Malyshev, S. A.; Babushkina, N. V. *ASDAM '98. Second International Conference on Advanced Semiconductor Devices and Microsystems*, 1998, 163–166.  
 (53) Gardner, R. F. G.; Sweett, F.; Tanner, D. W. *J. Phys. Chem. Solids* **1963**, *24*, 1175–1181.  
 (54) Orthner, H. R.; Roth, P. *Mater. Chem. Phys.* **2003**, *78*, 453–458.  
 (55) Chai, C. C.; Peng, J.; Yan, B. P. *Sens. Actuators, B* **1996**, *34*, 412–416.

- (56) Fonash, S. J. *J. Appl. Phys.* **1976**, *47*, 3597–3602.  
 (57) Shewchun, J.; Dubow, J.; Myszkowski, A.; Singh, R. *J. Appl. Phys.* **1978**, *49*, 855–864.  
 (58) Ishii, H.; Sugiyama, K.; Ito, E.; Seki, K. *Adv. Mater.* **1999**, *11*, 605–625.  
 (59) Untereker, D. F.; Lennox, J. C.; Wier, L. M.; Moses, P. R.; Murray, R. W. *J. Electroanal. Chem.* **1977**, *81*, 309–318.  
 (60) NIST XPS database: <http://srdata.nist.gov/XPS>.  
 (61) Cole, D. A.; Shallenberger, J. R.; Novak, S. W.; Moore, R. L.; Edgell, M. J.; Smith, S. P.; Hitzman, C. J.; Kirchhoff, J. F.; Principe, E.; Nieveen, W. *J. Vac. Sci. Technol., B* **2000**, *18*, 440.  
 (62) Minami, T. *J. Vac. Sci. Technol., A* **1999**, *17*, 1765.  
 (63) Batista, E. R.; Friesner, R. A. *J. Phys. Chem. B* **2002**, *106*, 8136–8141.  
 (64) Gunnarsson, M.; Jakobsson, A. M.; Ekberg, S.; Albinsson, Y.; Ahlberg, E. *J. Colloid Interface Sci.* **2000**, *231*, 326–336.

mM Co(NO<sub>3</sub>)<sub>2</sub> the cobalt loading is at most 10<sup>-8</sup> mol/cm<sup>2</sup> (60 atoms/nm<sup>2</sup> of the macroscopic electrode surface or 0.6  $\mu$ g/cm<sup>2</sup>). With an adsorption site density of about 2.5 sites/nm<sup>2</sup> for cobalt on hematite<sup>65</sup> this corresponds to a maximum of 24 atomic layers on a flat surface. Since the roughness factor of the hematite films (Figure 1) obtained by dye adsorption is 21  $\pm$  2, the real coverage is about a monolayer. This suffices to catalyze oxygen evolution from water by the valence band holes of hematite. Simple precipitation of Co(OH)<sub>2</sub> by dipping a 10 mM Co(NO<sub>3</sub>)<sub>2</sub>-treated electrode unrinsed into 1 M NaOH reduces the photocurrent, probably due to light absorption by excess cobalt. Also, heating a cobalt-activated electrode above 250 °C in air is detrimental, presumably due to aggregation of atomic cobalt sites into larger cobalt oxide clusters, decreasing the contact of the catalyst with the hematite surface and enhancing light absorption. This may also explain why cobalt oxide deposited by spray pyrolysis at 340 °C on sprayed  $\alpha$ -Fe<sub>2</sub>O<sub>3</sub> electrodes was found to reduce the photocurrent.<sup>20</sup>

The electrocatalytic activity of cobalt and iron/cobalt oxides and hydroxides for water oxidation is well established and involves the Co<sup>II</sup>/Co<sup>III</sup> and Co<sup>III</sup>/Co<sup>IV</sup> couples.<sup>66–70</sup> It has been pointed out that valence-band holes created by visible light illumination of  $\alpha$ -Fe<sub>2</sub>O<sub>3</sub> have mainly Fe<sup>IV</sup> rather than O<sup>2-</sup> 2p<sup>6</sup> character as in TiO<sub>2</sub>, resulting in a small rate constant for water oxidation.<sup>24</sup> On the cobalt-modified hematite surface holes may be trapped by Co<sup>II</sup> sites as Co<sup>III</sup>, which in turn can be oxidized by a second hole to Co<sup>IV</sup>. The distinct photocurrent at the beginning of the anodic scan of the cobalt-modified electrode (Figure 4b), decaying within seconds at constant potential and being absent in the dark and on the nonmodified electrode, can be attributed to such a photooxidation of surface cobalt sites.

Based on studies of water oxidation by transition metal oxides,<sup>70,71</sup> transition metal clusters,<sup>72,73</sup> the manganese cluster in natural photosynthesis<sup>74–76</sup> and TiO<sub>2</sub> photoanodes<sup>77</sup> the mechanism shown in Figure 5 is proposed as a working hypothesis. Stepwise oxidation of vicinal Co sites by photogenerated holes accompanied by proton abstraction from the surface hydroxyl groups in NaOH produces Co(IV) linked to strongly electrophilic oxo groups (Co<sup>IV</sup>=O) (S<sub>0</sub> to S<sub>4</sub>). Nucleophilic attack by hydroxide creates an O–O bond in the form of a peroxo intermediate (S<sub>4</sub>'). This releases dioxygen accompanied by hydrogen transfer to a vicinal oxo group. Rehydroxylation of the liberated Co<sup>II</sup> coordination site by the electrolyte closes the cycle. Hole trapping by surface Co sites thus allows accumulation of oxidation equivalents without formation of highly energetic intermediates such as OH radicals.

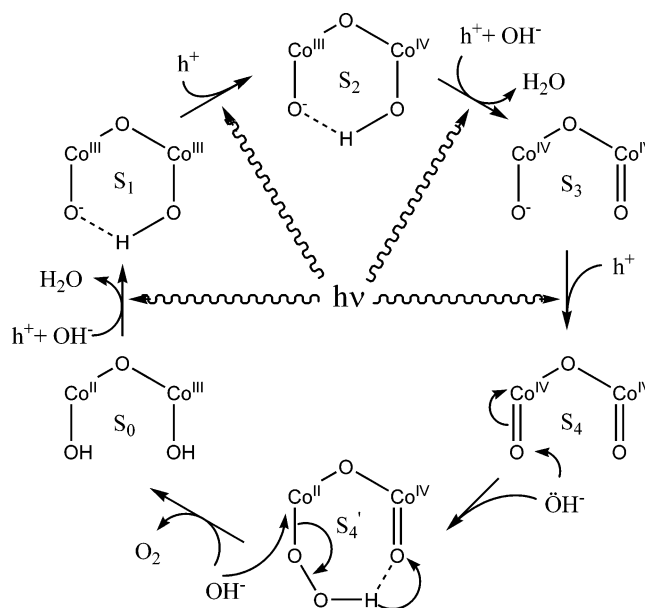


**Figure 5.** Mechanistic proposal for water photooxidation at the cobalt-modified hematite surface. (S<sub>0</sub> to S<sub>4</sub>): capture of four photogenerated holes by vicinal Co centers accompanied by deprotonation of surface hydroxyl groups creates highly electrophilic oxo groups on Co<sup>IV</sup>. Nucleophilic attack from hydroxide on one Co<sup>IV</sup>=O results in O–O bond formation and a peroxo intermediate (S<sub>4</sub>'). This decomposes to dioxygen under hydrogen transfer to the second Co<sup>IV</sup>=O. Rehydroxylation of the dangling Co<sup>II</sup> coordination site by the electrolyte closes the cycle. The same mechanism can be envisaged with Fe in place of Co.

The proposed water oxidation cycle comprising states S<sub>0</sub> to S<sub>4</sub> is analogous to that discussed for the oxygen evolving complex of photosystem II, which contains an oxygen bridged manganese cluster with two redox active Mn ions.<sup>75,76</sup> The same mechanism may be envisaged for a mixed Fe/Co as well as the unmodified Fe<sub>2</sub>O<sub>3</sub> surface ( $\mu$ -oxo bridged iron dimers also constitute the active site of several dioxygen activating enzymes and undergo valence changes from Fe<sup>II</sup> through Fe<sup>III</sup> to Fe<sup>IV</sup>).<sup>78</sup>

Other well-known oxygen evolution catalysts, such as Ru, Ni, and Mn, as well as binary<sup>79</sup> and ternary<sup>80</sup> mixtures of cobalt with other transition metals are presently being investigated in our laboratory.

**Photocurrent Action Spectra.** The incident photon to current efficiency as a function of wavelength for the hematite electrode of Figure 5 before cobalt treatment is shown in Figure 6a. Cobalt deposition enhances the IPCE by a factor of 1.2 between 350 and 500 nm and slightly more outside this region (Figure 6b). With IPCE = 36% at 400 nm and 42% at 370 nm and 1.23 V<sub>RHE</sub>, this electrode is much more efficient in water photooxidation than the best published Fe<sub>2</sub>O<sub>3</sub> thin films (IPCE = 25% at 400 nm and 1.42 V<sub>RHE</sub>)<sup>23</sup> and even better than the best reported niobium-doped  $\alpha$ -Fe<sub>2</sub>O<sub>3</sub> single crystals (IPCE = 37% at 370 nm and 1.23 V<sub>RHE</sub>).<sup>7,8</sup> The actual quantum efficiency is still higher since some light is lost by reflection at the uncoated electrochemical cell window and, due to the high refractive index of hematite, to a larger extent, at the electrolyte/Fe<sub>2</sub>O<sub>3</sub> interface.<sup>6</sup>

(65) Jeon, B. H.; Dempsey, B. A.; Burgos, W. D.; Royer, R. A.; Roden, E. *Water Res.* **2004**, *38*, 2499–2504.

(66) Brunschwig, B. S.; Chou, M. H.; Creutz, C.; Ghosh, P.; Sutin, N. *J. Am. Chem. Soc.* **1983**, *105*, 4832–4833.

(67) Schmidt, T.; Wendt, H. *Electrochim. Acta* **1994**, *39*, 1763–1767.

(68) Matsumoto, Y.; Sato, E. *Mater. Chem. Phys.* **1986**, *14*, 397–426.

(69) Behl, W. K.; Toni, J. E. *J. Electroanal. Chem.* **1971**, *31*, 63–75.

(70) Elizarova, G. L.; Zhidomirov, G. M.; Parmon, V. N. *Catal. Today* **2000**, *58*, 71–88.

(71) Rossmeisl, J.; Logadottir, A.; Nørskov, J. K. *Chem. Phys.* **2005**, *319*, 178–184.

(72) Ruttinger, W.; Dismukes, G. C. *Chem. Rev.* **1997**, *97*, 1–24.

(73) Binstead, R. A.; Chronister, C. W.; Ni, J.; Hartshorn, C. M.; Meyer, T. J. *J. Am. Chem. Soc.* **2000**, *122*, 8464–8473.

(74) Ferreira, K. N.; Iverson, T. M.; Maghlaoui, K.; Barber, J.; Iwata, S. *Science* **2004**, *303*, 1831–1838.

(75) McEvoy, J. P.; Gascon, J. A.; Batista, V. S.; Brudvig, G. W. *Photochem. Photobiol. Sci.* **2005**, *4*, 940–949.

(76) Dau, H.; Haumann, M. *Photosynth. Res.* **2005**, *84*, 325–331.

(77) Nakamura, R.; Okamura, T.; Ohashi, N.; Imanishi, A.; Nakato, Y. *J. Am. Chem. Soc.* **2005**, *127*, 12975–12983.

(78) Kryatov, S. V.; Rybak-Akimova, E. V.; Schindler, S. *Chem. Rev.* **2005**, *105*, 2175–2226.

(79) Wu, G.; Li, N.; Zhou, D.-R.; Mitsuo, K.; Xu, B.-Q. *J. Solid State Chem.* **2004**, *177*, 3682–3692.

(80) Singh, R. N.; Singh, N. K.; Singh, J. P. *Electrochim. Acta* **2002**, *47*, 3873–3879.



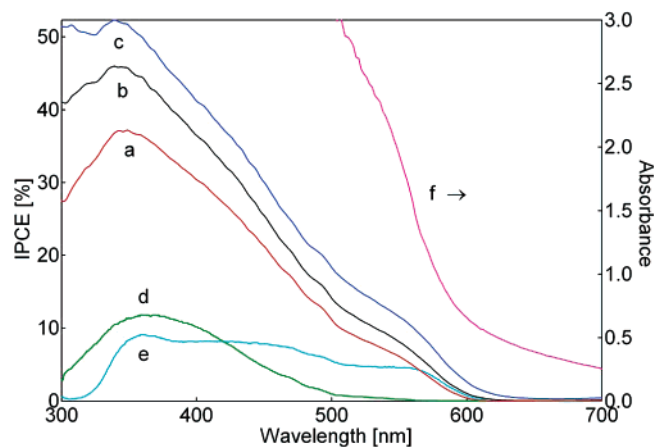


**Figure 6.** Incident photon to current efficiency (IPCE) spectrum of the same electrode as in Figure 4. (a) Unmodified  $\text{Fe}_2\text{O}_3$  at 1.23  $V_{\text{RHE}}$ ; (b) after cobalt deposition, at 1.23  $V_{\text{RHE}}$ ; (c) at 1.43  $V_{\text{RHE}}$ ; (d) at 1.03  $V_{\text{RHE}}$ ; (e) at 1.23  $V_{\text{RHE}}$  but illuminated through the  $\text{SnO}_2$  substrate; (f) absorption spectrum of this electrode.

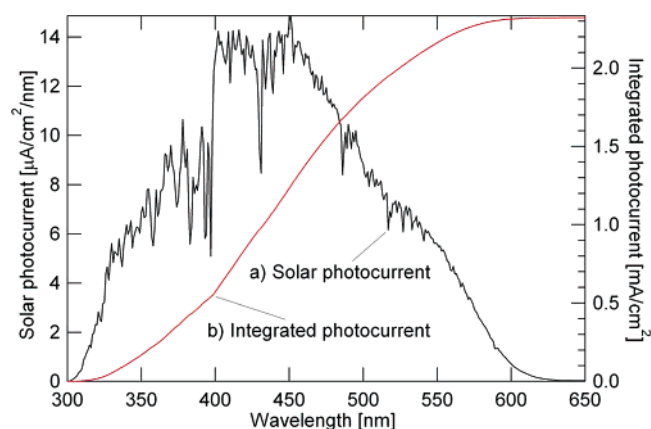


**Figure 7.** (a) Solar photocurrent spectrum of the cobalt-treated  $\text{Fe}_2\text{O}_3$  electrode at 1.23  $V_{\text{RHE}}$  obtained by multiplication of its IPCE spectrum (Figure 6b) with the photon flux spectrum of global sunlight (1000  $\text{W}/\text{m}^2$  AM 1.5 G). (b) Total photocurrent under global sunlight between 300 nm and a given wavelength (integral of curve a).

Multiplication of the IPCE spectrum with the photon flux obtained from the spectral irradiance  $E(\lambda)$  for global sunlight (1000  $\text{W}/\text{m}^2$  AM 1.5 G)<sup>47</sup> yields the solar photocurrent spectrum (Figure 7a):

$$I(\lambda) = \text{IPCE} \cdot E(\lambda) \cdot \lambda \cdot e/hc$$

The total photocurrent under global sunlight is obtained by integration over the spectrum (Figure 7b)<sup>6</sup>

$$\int I(\lambda) d\lambda = 2.3 \text{ mA}/\text{cm}^2$$

A measurement under natural global sunlight was done on a day with a cloudless sky but slight haze (Lausanne, Switzerland, latitude 46.5° N, longitude 6.5° E, at 10 a.m. summertime on 7 June 2006, corresponding to a zenith angle of 48.6° or AM 1.51). At an irradiance of 930  $\text{W}/\text{m}^2$  (measured with a thermopile Kipp & Zonen CM5) the photocurrent density of the  $\text{Fe}_2\text{O}_3$  electrode facing the sun was 2.05  $\text{mA}/\text{cm}^2$  at 1.23  $V_{\text{RHE}}$ , corresponding to 2.2  $\text{mA}/\text{cm}^2$  at 1000  $\text{W}/\text{m}^2$  AM 1.5 G. The calculated (2.3  $\text{mA}/\text{cm}^2$ ) and measured (2.2  $\text{mA}/\text{cm}^2$ ) photocurrent for natural sunlight are lower than that measured under simulated sunlight (Figure 5b: 2.7  $\text{mA}/\text{cm}^2$ ). The dif-

ference is due to a spectral mismatch of the xenon lamp which exhibits a higher photon flux in the UV than the sun.<sup>6, 81</sup>

Previously claimed higher photocurrents for sprayed  $\text{Fe}_2\text{O}_3$  films under simulated sunlight (3.3  $\text{mA}/\text{cm}^2$  at 1.23  $V_{\text{RHE}}$ , 7  $\text{mA}/\text{cm}^2$  at 1.67  $V_{\text{RHE}}$ )<sup>82</sup> are unrealistic in view of the action spectra reported by the authors (IPCE = 20% at 400 nm and 1.67  $V_{\text{RHE}}$ ) and could not be reproduced by others.<sup>5,23</sup> Such high currents may, however, be obtained with a mercury–xenon lamp instead of the sun as the light source.<sup>6</sup>

The photocurrent onset around 600 nm (Figure 6b) coincides with the onset of strong light absorption (Figure 6f) and corresponds to the 2.1 eV indirect band gap of  $\alpha\text{-Fe}_2\text{O}_3$ .<sup>5</sup> However, the efficiency rises much more slowly and reaches its maximum only at 350 nm, although more than 90% of the incident light is absorbed below 570 nm. This indicates that more energetic photons have a higher quantum efficiency for charge separation, which can be explained by their shorter penetration depth in  $\text{Fe}_2\text{O}_3$ . Short wavelength light creates electron/hole pairs in the outer part of the hematite film constituted of nanoparticles with close contact to the electrolyte. Charge separation is efficient, since these holes need to diffuse less than 10 nm to reach the  $\text{Fe}_2\text{O}_3$  surface and react with water.

At an electrode potential of 1.43  $V_{\text{RHE}}$  (Figure 6c) instead of 1.23  $V_{\text{RHE}}$  the relative IPCE enhancement is higher in the long wavelength tail (by a factor of 1.42 at 550 nm) than at shorter wavelength (1.13 times at 350 nm). At only 1.03  $V_{\text{RHE}}$  light above 500 nm produces nearly no photocurrent (Figure 6d). This can again be explained by the longer penetration depth of less energetic photons, creating electron/hole pairs deep inside the  $\text{Fe}_2\text{O}_3$  film and far away from the electrolyte interface. Such holes can reach the surface by diffusion only if their recombination with electrons is prevented by stronger electron depletion achieved at more positive polarization. According to this interpretation the higher efficiency at short wavelengths is not necessarily due to the stronger oxidizing power of valence band holes at oxygen sites generated by direct  $\text{O}^{2-} 2p^6 \rightarrow \text{Fe}^{3+} 3d$  transitions ( $\lambda < 400$  nm) as compared to  $\text{Fe}^{4+}$  holes due to indirect  $\text{Fe}^{3+} 3d \rightarrow 3d$  transitions ( $\lambda < 620$  nm).<sup>24,25</sup>

Backside illumination of the hematite film through the  $\text{SnO}_2$  glass substrate gives a much lower IPCE (Figure 6e), approaching that for frontside illumination from the electrolyte side only in the long wavelength tail (the drop below 340 nm is due to light absorption by the glass substrate). This is in contrast to photooxidation of  $\text{SCN}^-$  at colloidal  $\text{TiO}_2$  films,<sup>83</sup> which show the highest charge separation efficiency for carriers created near the back contact with the  $\text{SnO}_2$  substrate. One difference of APCVD hematite films compared to colloidal  $\text{TiO}_2$  electrodes is their dendritic morphology, with a more compact stem next to the substrate and a highly branched nanostructure toward the electrolyte (Figure 1A). Another difference is the much shorter hole diffusion length in  $\alpha\text{-Fe}_2\text{O}_3$  (20 nm,<sup>24</sup> 2–4 nm<sup>25</sup>) compared to  $\text{TiO}_2$  (800 nm).<sup>83</sup> Since backside illumination creates holes mostly in the more compact part of the  $\text{Fe}_2\text{O}_3$  film near the  $\text{SnO}_2$  substrate and their diffusion length is so short, they have a lesser chance reaching the electrolyte interface and oxidize water. Only in the long wavelength tail the light is equally

(81) Seaman, C. H. *Solar Energy* **1982**, 29, 291–298.

(82) Miller, E. L.; Rocheleau, R. E.; Khan, S. *Int. J. Hydrogen Energy* **2004**, 29, 907–914.

(83) Sodergren, S.; Hagfeldt, A.; Olsson, J.; Lindquist, S. E. *J. Phys. Chem.* **1994**, 98, 5552–5556.

absorbed throughout the film thickness so that the efficiency is independent of the illumination side.

### Conclusions

Deposition of silicon-doped nanocrystalline hematite films by APCVD produces Fe<sub>2</sub>O<sub>3</sub> photoanodes that oxidize water under visible light with unprecedented efficiency. The dendritic nanostructure minimizes the distance photogenerated holes have to diffuse to the Fe<sub>2</sub>O<sub>3</sub>/electrolyte interface in a film that is thick enough for strong light absorption. The efficiency is further enhanced by deposition of a thin insulating SiO<sub>2</sub> layer below and a cobalt monolayer on top of the Fe<sub>2</sub>O<sub>3</sub> film.

**Acknowledgment.** We wish to thank V. Shklover for XRD characterization of our films, N. Xanthopoulos for XPS analysis, R. Humphry-Baker for advice with light calibration, the Centre Interdisciplinaire de Microscopie Electronique for assistance in SEM imaging, P. Stadelmann for performing and interpreting the XEDS/TEM elemental analysis, and C.M. Eggleston for many inspiring discussions. Financial support from the Swiss Federal Office of Energy (SFOE) and Hydrogen Solar Ltd. is gratefully acknowledged.

JA064380L